

# Selective Growth and Directed Integration of ZnO Nanobridge Devices on Si Substrates without a Metal Catalyst Using a ZnO Seed Layer

JOHN F. CONLEY, JR.,<sup>1,2</sup> LISA STECKER,<sup>1</sup> and YOSHI ONO<sup>1</sup>

1.—IC Process Technology Laboratory, Sharp Labs of America, 5700 NW Pacific Rim Blvd., Camas, Washington, 98607. 2.—E-mail: jconley@sharplabs.com

Directed assembly and integration of ZnO nanobridges (NBs) into working devices on Si substrates was achieved. Metal catalysts were not used, and the “harvest and disperse” method of nanorod (NR) integration was avoided. High-quality ZnO NRs were grown via a vapor–solid method selectively on a patterned thin-film ZnO seed layer. ZnO NRs exhibited a single-crystalline structure with c-axis preferred orientation, were aligned roughly perpendicular to the surface, and showed a strong intrinsic near-band edge photoluminescence peak at 380 nm with no detectable visible photoluminescence. These ZnO NRs were grown to span gaps between separated electrodes, terminate on an opposing surface, and effectively form electrically accessible vertical or horizontal ZnO NB devices. Operation of the directly grown horizontal ZnO NB devices as gas and UV sensors was performed, demonstrating a significant step toward practical large-scale integration of nanodevices into Si microelectronics.

**Key words:** Nanotechnology, ZnO, sensor, luminescence, directed assembly, selective growth

## INTRODUCTION

ZnO is an attractive material for nanorod (NR)-based electronics, UV photonics, and sensing applications.<sup>1–17</sup> Because the gas-sensing properties of ZnO and other metal oxides are known to be dominated by surface charge-exchange reactions with adsorbants,<sup>3</sup> the inherently large surface-to-volume ratio of nanostructured materials offers the promise of enhanced sensitivity.<sup>3,18</sup> Due to the current domination of CMOS technology, in order to take full advantage of nanomaterials, integration into Si-based microelectronics devices will be necessary. Currently, the most widely used method of nanomaterial integration is one in which the ZnO NRs are “harvested” from a growth substrate, placed into solution, and then dispersed randomly onto the device substrate. Placement can be assisted by electric fields and fluidic flow, etc. Although much excellent work has recently been performed using this method, such as the formation and testing of individual ZnO NR devices and their sensitivity to ultraviolet (UV)

light, O<sub>2</sub>, H<sub>2</sub>O, ethanol, CO, NO<sub>2</sub>, NH<sub>3</sub>, etc.,<sup>4–6,10–18</sup> with drawbacks such as random placement, contamination, and general incompatibility with Si processing, the “harvest and disperse” method is not considered to be suitable for large-scale manufacturing. A more elegant approach would be to selectively grow nanostructures directly onto desired areas of a substrate. Although this also has been recently been achieved by many groups,<sup>19–23</sup> an even more practical method would be to grow NRs directly from one desired location to another desired location, such as between two electrodes. Although a few groups have very recently reported using this approach to fabricate nanobridge (NB) structures,<sup>24–26</sup> the Hewlett Packard (Palo Alto, CA) group was the first and only to use a semiconductor, successfully growing Si NBs across a trench on a Si substrate.<sup>26</sup> Unfortunately, the HP technique, along with almost all of the above selective growth techniques, suffers from a reliance on the use of metal catalysts such as Au or Ti to initiate and define regions of vapor–liquid–solid (VLS)<sup>27</sup> growth. Metal catalysts, which are generally difficult to subtractively pattern

and can be a source of detrimental contamination (i.e., deep levels in Si), are best avoided in a Siprocess.

In this work, we first show how ZnO NRs can be grown selectively on a Si substrate without a metal catalyst. Growth of high-quality ZnO NRs takes place selectively on ZnO thin-film seed regions via a vapor–solid (VS) growth mechanism<sup>17,28</sup> rather than a VLS mechanism. Scanning and transmission electron microscopy (SEM and TEM) along with x-ray diffraction (XRD) measurements showed that the NRs exhibit alignment perpendicular to the growth surface and a single-crystalline structure with high c-axis preferred orientation. Photoluminescence (PL) measurements reveal a sharp near-band edge intrinsic UV PL peak at  $\sim 380$  nm without any of the broad, visible PL known to be due to defects. Using this ZnO seed layer selective growth technique, we demonstrate a repeatable method for directed assembly and integration of ZnO NRs into working NB devices on silicon-on-insulator (SOI) substrates. Atomic layer deposition (ALD) was used to deposit a thin film ZnO seed layer conformally onto the side walls of SOI trench structures and ceilings and floors of undercut SOI island structures. Self-assembled ZnO NRs were then grown on the patterned ZnO seed layer to span trench and ceiling-to-floor gaps and self-terminate on opposing surfaces, effectively forming horizontal and vertical ZnO NBs. Operation of the horizontal ZnO NB devices as gas and UV sensors was achieved, demonstrating the potential of this method for practical large-scale integration of nanodevices into Si microelectronics.

## EXPERIMENTAL DETAILS

Thin-film seed layers of ZnO were deposited on Si wafers using either atomic layer deposition (ALD) or metalorganic spin-on-deposition (MOD). Prior to seed layer deposition, Si wafers were cleaned and then etched in a dilute HF solution to remove any native oxide and produce a hydrogen-terminated surface. For the ALD process, 4- to 40-nm-thick ZnO films were deposited using alternating pulses of diethylzinc (DEZ) precursor and H<sub>2</sub>O vapor at substrate temperatures between 140 and 170°C.<sup>29</sup> For the MOD process, 80 nm of ZnO was deposited using zinc acetate dehydrate in 2-methoxyethanol and ethanolamine. To drive off residual solvent, the as-coated MOD film was baked at 100, 200, and 300°C for 1 min. at each temperature, and then underwent rapid thermal anneal (RTA) steps in dry air at 500°C for 2 min. and at 1000°C for 5 min. Both ALD and MOD ZnO films are polycrystalline. ZnO films are patterned by etching in 50:1 HF for about 10 s using a photolithographically defined photoresist mask.

ZnO nanostructure growth was performed in a 5-cm diameter quartz tube furnace by exposing substrates to Zn vapor at 800–915°C for approximately 30 min. with a flow of 30–80 sccm Ar and a trace amount of oxygen.<sup>17</sup> Zn vapor is generated through

carbo-thermal reduction of ZnO powder using equal parts ZnO and graphite.<sup>2</sup> For the growth conditions used, a white powdery growth region approximately 3–4 cm long is observed beginning approximately 7–8 cm from the source.

Construction of NB devices began by etching Si islands (after an initial n<sup>+</sup> implantation: P, 100 keV,  $6 \times 10^{15}/\text{cm}^2$ ) on the SiO<sub>2</sub> buried oxide (BOX) layer of a silicon-on-insulator (SOI) substrate (see below, Fig. 11a). In order to form vertical NBs, the buried oxide layer between the Si islands is dry etched down to the Si substrate, and then wet etched using HF to undercut the Si islands (see below, Fig. 12a). Next, a highly conformal thin ZnO seed layer is deposited via ALD. (Unlike traditional chemical vapor deposition, ALD precursors are pulsed alternately into the deposition chamber and are separated by purges. Reactions take place on the substrate surface and are self-limiting. The self-limiting nature of the process allows for uniformity and excellent conformality with film thickness precisely controlled by the number of precursor pulse/purge cycles.) After a photolithographic step and dry etch, ZnO is left coating only vertical surfaces and areas under the Si islands.

SEM images were taken using a 6400F JEOL (Peabody, MA) instrument with a tungsten filament, XRD measurements were made using a Philips X'Pert system (Almelo, the Netherlands), and TEM images were obtained using an FEI Tecnai F-20 (Philips Electron Optics, Holland) field-emission (200-kV) microscope. Room temperature PL spectra were taken on an Accent Optical Technologies (Bend, OR) RPM200 equipped with a  $\sim 3.5$  mW quadrupled Nd:YAG laser (266 nm) passed through a 295-nm low-pass filter. The luminescence was dispersed through a 600 g/mm grating blazed at 400 nm and detected by a back-thinned, TE-cooled CCD.

## RESULTS

### Selective Growth

In our investigations of VLS growth of ZnO nanostructures, we often noticed excellent nucleation of ZnO NRs on downstream ZnO particles. Shown in the SEM image in Fig. 1, these “porcupines” were the inspiration for the use of thin film ZnO as a seed layer for selective growth without a metal catalyst.

Various methods were used to deposit thin films of ZnO on (100)Si substrates. As illustrated in Fig. 2, the ZnO was then patterned and subjected to the NR growth procedure. SEM images in Figs. 3 and 4 demonstrate that growth of ZnO NRs occurred selectively on patterned  $\sim 6$  nm of ALD ZnO and 80 nm of MOD ZnO, respectively.

As shown in Fig. 5, selective growth of ZnO NRs on Si was also observed on 10- to 35-nm-thick Al-doped ZnO:Al thin films, opening the possibility of a conductive seed layer. The NRs in Fig. 5 were grown at 800°C.

Figures 3a–3c and 4 show ZnO NRs from near the center of the growth region that are vertically oriented and fairly well aligned with one another.

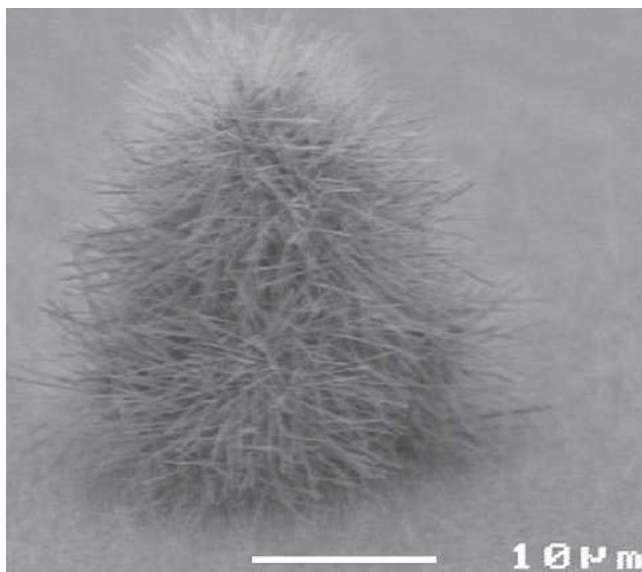


Fig. 1. SEM image of ZnO NR growth on a downstream ZnO particle.

SEM resolution in these images was too low to determine whether the NRs have a hexagonal cross section. The NRs do not appear to taper and do not appear to have catalyst “balls” at the top end. The absence of the catalyst balls suggests that a VLS mechanism is not responsible for growth but that NR growth takes place via a vapor transport/solid condensation mechanism, with the ZnO film acting as a seed layer for nucleation. Although catalyst-free growth on Si has previously been shown, selectivity on Si was not achieved.<sup>12,30–32</sup>

Comparison of the NRs in Fig. 3a–3c with those in Fig. 4 reveals a slight variation in morphology, demonstrating that different methods of depositing the same seed material may be used to tailor NR morphology. The dark shadow-like border around the NRs in Fig. 4 has been identified as Zn silicate. The silicate phase was found to form at the ZnO/Si interface when ZnO thin films were annealed above 950°C. It remains around the pattern border because it is more resistant than ZnO to HF etching. Although the Zn silicate does not seed ZnO NR growth, it may impact morphology. Shown in Fig. 3d is an image of NRs on the 6-nm ALD ZnO film from a part of the growth region that lies closer to the source. It is seen that these NRs are more sparsely distributed and not as well aligned. Larger-diameter, hexagonally shaped NRs have also been observed (see Fig. 12). In general, we have found that within the NR growth region, morphology varies as a function of distance from the source. In the simple 1.5-in. diameter tube furnace used to

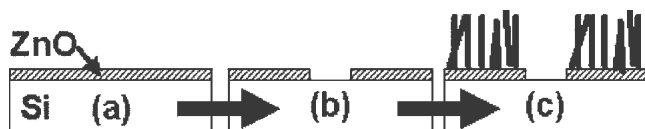


Fig. 2. (a) Deposition and (b) patterning of a thin ZnO seed layer on a Si substrate followed by (c) selective growth of ZnO NRs.

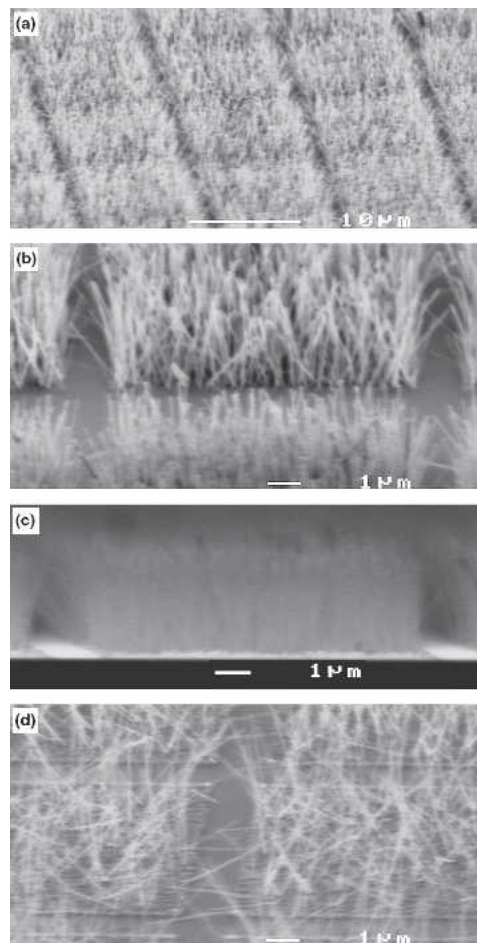


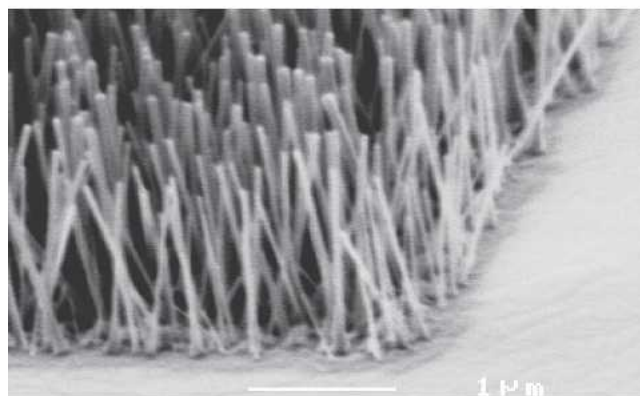
Fig. 3. SEM images showing selective growth of ZnO NRs on patterned 6-nm-thick ALD ZnO.

grow the NRs, gas flow is not well controlled. It is likely that the limited growth region and much of the morphology variation is due to variations in gas flow, temperature, and precursor arrival rate. Other groups have also reported that growth is sensitive to these factors.<sup>22,32</sup>

Other factors that may impact NR morphology are differences in ZnO seed layer crystallinity (brought about by either the deposition method or anneal conditions performed before NR growth), the method of supplying Zn vapor, and preparation of the Si surface prior to thin film deposition and nanostructure growth. Shown in Fig. 6 are SEM images of NR growth on a blanket ALD ZnO film deposited over alternating regions of  $n^+$  implanted (As,  $3 \times 10^{15}/\text{cm}^2$ , 60 keV), unimplanted, and  $p^+$  implanted ( $\text{BF}_2$ ,  $2.5 \times 10^{15}/\text{cm}^2$ , 45 eV) Si. Implants were followed by a 30-min, 800°C activation anneal. Nanostructure morphology was observed to be dependent upon substrate ion implantation. NRs on the implanted regions appear densely packed, thick, and hexagonal while on the unimplanted regions NRs are thin and more sparsely distributed. As  $n^+$  and  $p^+$  regions show similar nanostructure morphology, it is likely that the difference is due to physical implant damage rather than a chemical effect.



(a)



(b)

Fig. 4. SEM images showing selective growth of ZnO NRs on patterned 80-nm-thick MOD ZnO.

Although NR morphology is a strong function of flow and other parameters, selectivity does not appear to be. As seen in Fig. 3, selective growth was observed everywhere on the samples that nanostructure growth occurred, independent of morphology. In no-growth areas amidst the growth region, there does not appear to be any film or randomly nucleated wires. However, note that nucleation is often observed at any severe surface anomaly such as a scratch and, as shown in Fig. 1, “porcupine” like nucleation is occasionally observed on ZnO particles that have traveled downstream from the powdered precursor.

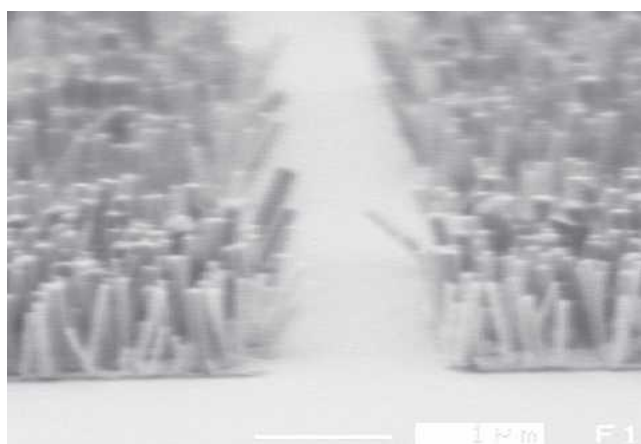
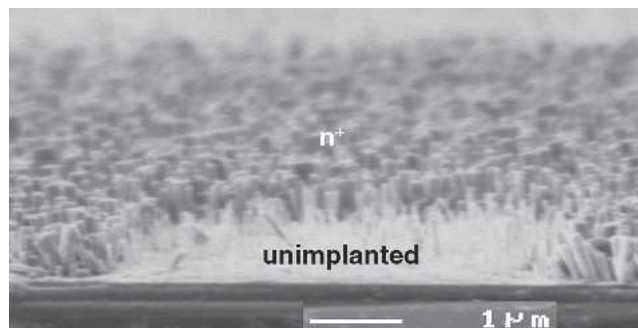
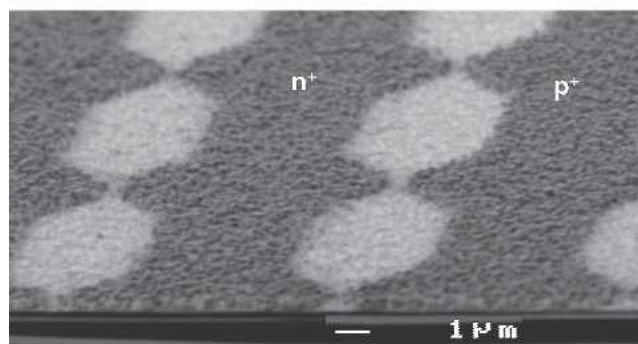


Fig. 5. SEM image showing selective growth of ZnO NRs on a patterned ZnO:Al seed layer.



(a)



(b)

Fig. 6. SEM images of ZnO NR grown on blanket ALD ZnO showing morphology variation due to substrate ion implantation. Dark regions are implanted, light regions are unimplanted.

### ZnO NR Properties

To examine crystal quality, XRD measurements were made on ZnO NRs grown (915°C for 30 min.) on either 35- or 7-nm-thick blanket ALD ZnO films. For the 35-nm thin-film region, the XRD pattern shown as line (a) in Fig. 7 corresponds to randomly oriented polycrystalline hexagonal wurtzite phase of ZnO. The same peak positions are observed as line (b) in Fig. 7, the NR growth region of this same sample, but the (002) peak is relatively much more intense, indicating a preferred c-axis orientation. Based upon the Scherrer equation, the average grain size in the 35-nm ZnO film approaches the thickness of the film. For the NR region, the Scherrer formula yields a grain size 3× to 10× larger.

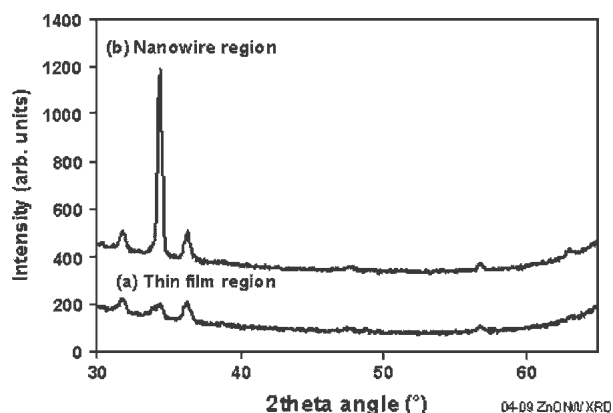


Fig. 7. XRD patterns for (a) the thin-film region and (b) the NR region for a 35-nm ALD ZnO seed layer.

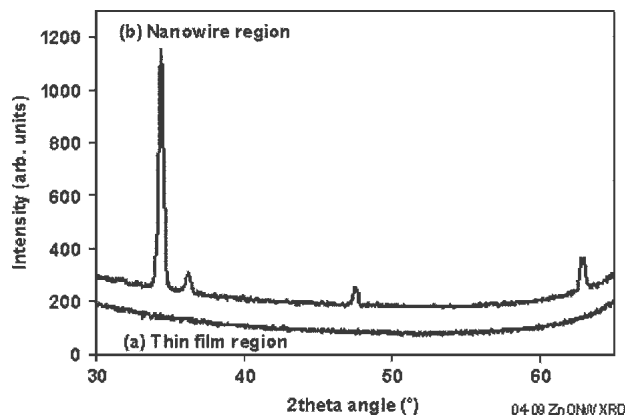


Fig. 8. XRD patterns for (a) the thin-film region and (b) the NR region for a 7-nm ALD ZnO seed layer.

Shown in Fig. 8 are XRD patterns for (a) the smooth thin film region and (b) the NR growth region for the 7 nm seed layer sample. For (a), the 7-nm ZnO thin-film region, the hexagonal phase is not detectable, while for (b), the NR growth region, a c-axis preferred orientation is clearly observed. The detection of the c-axis preferred phase in these samples is an indication of the high crystal quality of the NRs. A Scherrer calculation for the NR on the 7-nm thin-film yields a grain size about equal to that obtained for the NR on the 35-nm film.

In order to further examine the internal structure of the NRs, TEM images were obtained on ZnO NRs that were grown on ~80 nm of spin-on ZnO and then dispersed onto a holey carbon grid. Although an selective area electron diffraction pattern was not obtained, the high-resolution TEM images in Figs. 9(a) and 9(b) show clear lattice planes, strongly suggesting that the ZnO NRs are single crystalline. The lower resolution TEM image in Fig. 9(c) does not reveal the presence of catalyst “balls” at the end of the wires, further evidence that growth takes place via a vapor–solid mechanism.

Room temperature PL spectra were taken on ZnO NRs grown on a 7-nm ALD ZnO thin-film seed layer. Shown in Fig. 10(a), a PL spectrum in the range of

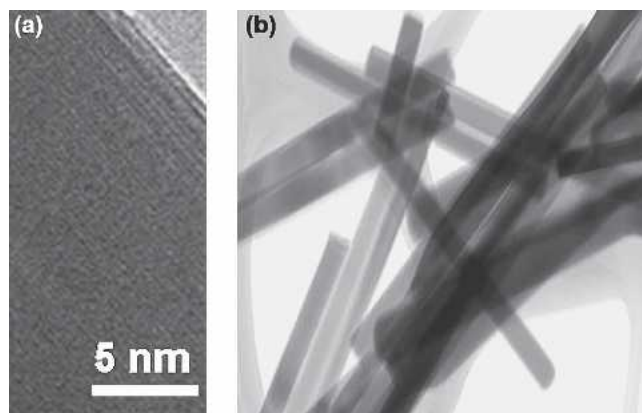


Fig. 9. (a) High-resolution and (b) low-magnification TEM images of ZnO NRs selectively grown on an 80-nm MOD ZnO film and them dispersed onto a holey carbon grid.

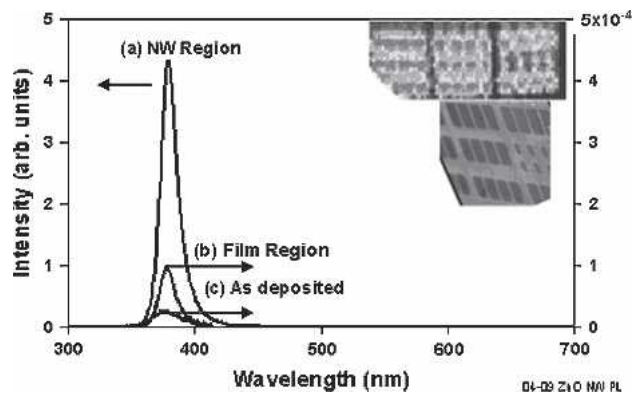


Fig. 10. PL spectra of (a) NR growth region (left axis), (b) no-growth region (right axis), and (c) as-deposited 35-nm ALD ZnO thin film (right axis). (Insets) Map of 380-nm PL intensity (top) and SEM image of same area (bottom).

300–700 nm reveals excellent characteristics with a strong emission peak at 380 nm. No trace of emission was detected in either the green or orange regions, indicating low densities of oxygen vacancies and other defects.<sup>33</sup> The 380-nm peak is due to an intrinsic near-band-edge recombination. The presence of a strong intrinsic PL peak combined with the absence of any extrinsic PL provides further evidence of the high crystal quality of the NRs.

Plotted on the right axis, similar (380-nm PL peak with no PL at visible wavelengths), but much weaker PL spectra are seen in (b) the no-growth region and (c) the as-deposited 35-nm ALD ZnO thin film. Post-deposition high-temperature annealing of the ZnO films was observed to increase PL intensity. Note that the PL intensity in the no-growth region is stronger than the as-deposited region due to the 30-min. 915°C heat cycle. The 380-nm PL peak in NR growth region is up to 10<sup>4</sup> times more intense than the no growth film region. For a 35.2-nm ALD ZnO seed layer (not shown), the 380-nm peak in the NR regions was found to be ~10× more intense than the thin-film regions. The intensity of the 380-nm peak in the NR regions is roughly equivalent for both samples. Similar results were observed for ZnO NRs grown on MOD ZnO seed layers.

A spatially resolved PL map of ZnO NRs grown on a patterned 6-nm ALD ZnO seed layer is shown as the top inset in Fig. 10. The contrast in this map corresponds to the intensity of the 380-nm peak (dark shading (red) indicates high intensity; light shading

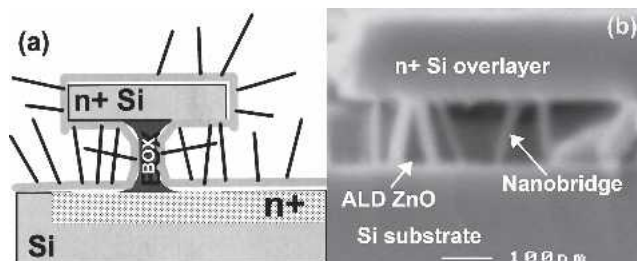


Fig. 11. Schematic sketch (a) and cross-sectional SEM (b) of vertical ZnO NBs spanning an undercut Si island.

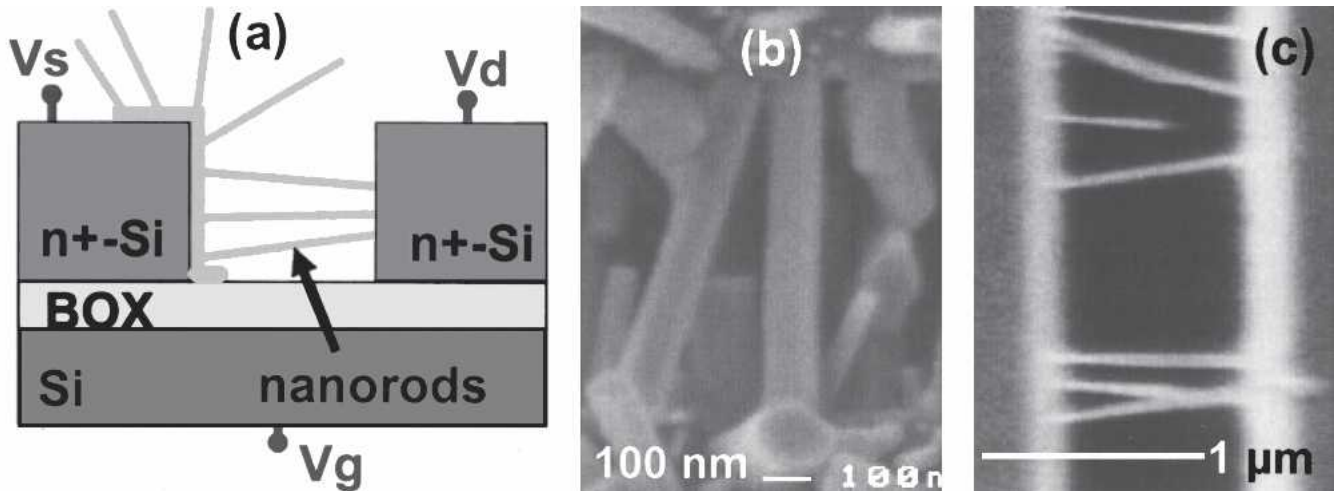


Fig. 12. Sketch (a) and top view SEMs (b, c) of horizontal ZnO NBs spanning a trench structure.

(blue) indicates low intensity). The three rows of dark dots in this image match the large dark squares ( $100 \mu\text{m} \times 100 \mu\text{m}$ ) in the off-normal SEM image below it. The dark squares are regions coated with ALD ZnO. Strong PL intensity is seen where the NR growth has occurred (red dots/dark squares). Blurriness in the PL map is due to the resolution limit of the PL instrument.

### ZnO Nanobridge Growth and Device Formation

As shown in Figs. 3–6, ZnO nanostructures initiate selectively on ZnO thin-film seed regions and grow roughly perpendicular to the surface.<sup>17</sup> When special structures such as those shown in Figs. 11a and 12a are coated with a conformal layer of ZnO deposited via ALD, growth of ZnO NW can be directed to span gaps and terminate on an electrode surface to form NBs. Figures 11b and 12b show SEM images of self-assembled vertical and horizontal NB structures. For the case of the horizontal structure, ZnO was left only on one wall so that the NBs terminate on Si. For the undercut vertical structure, the NBs terminate on ZnO. Although it is evident that ZnO was not patterned for the vertical structure, it could easily have been etched to leave ZnO only in the recessed region. By virtue of the self-assembled connection between the two terminals, NBs are automatically integrated into an electrically accessible device structure. Fairly high densities of NBs can be grown between the two terminals, allowing a large surface area of ZnO to be exposed to an ambient and enabling the possibility of high sensitivity. NBs were 10–100 nm in diameter and spanned gaps of up to several micrometers.

### ZnO Nanobridge Device Operation

$I_{sd}$ – $V_{sd}$  measurements on a  $0.8\text{-}\mu\text{m}$  horizontal comb structure (inset) before and after NB growth for  $V_g$  stepped from  $-5$  to  $+3$  V in  $2\text{-V}$  increments are shown in Fig. 13. Prior to NW growth, leakage through the structure was below measurement sen-

sitivity (4156C using medium integration time) indicating that the BOX is very effective at isolating the terminals. After NW growth, a large current can be measured between the  $n^+$  Si islands, demonstrating that the ZnO NBs make electrical connection to both terminals. The horizontal bridge structure can be operated as a three-terminal device.  $V_g$  appears to have a weak gating effect on the ZnO channel (inset) of these nonoptimized devices. The weak gate effect appears to be larger for longer bridge gaps and can likely be increased through optimization. Sweeping  $V_{sd}$  to breakdown (not shown) resulted in a decrease of 2 orders of magnitude in current rather than a short circuit, further evidence of conduction through the NBs. The  $I$ – $V$  curves in Fig. 13 represent the behavior of many wires in parallel. The observed poor contact resistance,  $R_c$ , is due primarily to the fact that measurements were made by probing directly to the Si pads without metallization. The high temperatures used for NW growth that made pregrowth metallization impossible and the small sample size limit for NW growth in the  $5\text{-cm}$  tube furnace which

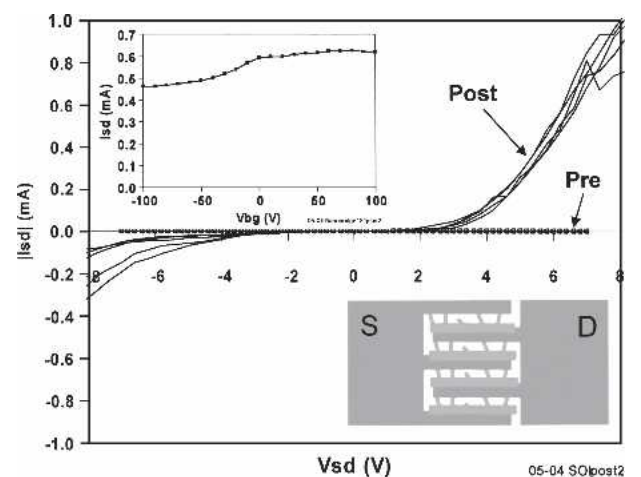


Fig. 13. Plot of  $I_{sd}$  vs.  $V_{sd}$  for  $V_g$  stepped from  $-5$  to  $3$  V in  $2\text{-V}$  increments for a  $0.8\text{-}\mu\text{m}$  gap comb structure (top view schematic shown in inset), pre (a) and post (b) ZnO NB growth. (Inset) Plot of  $I_{sd}$  vs.  $V_g$  for  $V_{sd} = 10$  V.

made post-growth conventional lithography impossible. Another source of  $R_c$  lies at the termination points of the nanobridges. The difference in initiation on ZnO and termination on Si may also account for some of the nonsymmetry in the I–V. Due to the large probe-to-pad  $R_c$ , these effects are currently difficult to isolate. We are investigating low-temperature NW growth methods that will allow full wafer processing and thus subsequent metallization that should improve probe-to-pad  $R_c$ .

Shown in Fig. 14 is a plot of  $I_{sd}$  vs. time for a 0.8- $\mu\text{m}$  gap comb structure operated in air under fluorescent/natural lighting with  $V_{sd} = 10\text{ V}$  and  $V_g = 0\text{ V}$ . At  $t = \sim 64\text{ s}$ , the sample was exposed to a the beam of a 375 nm UV pen light. The UV light resulted in an immediate 1 to 2 order of magnitude increase in current to the mid- $10^{-3}\text{ A}$  range. In addition to band-to-band generation of carriers, it is thought that the large UV response is also due to rapid desorption of all surface species. As soon as the UV light was removed at  $t = 71\text{ s}$ , an extended recovery period (about 300 s) begins in which the current slowly decreases back to pre-exposure value. As response magnitude and recovery time depended on ambient conditions, this extended recovery period is likely due to the slow re-adsorption of surface species. ZnO is known to be sensitive to UV light, and UV illumination has been used to improve recovery time in metal oxide sensors. The UV response under these nonideal experimental conditions is qualitatively consistent with reports for ZnO NR devices fabricated via the pick-and-place method.<sup>4,5,10,14</sup>

Plots of  $I_{sd}$  as a function of time for a 0.6- $\mu\text{m}$  comb structure operated with the microscope lamp on,  $V_{sd} = 15\text{ V}$ , and  $V_g = 10\text{ V}$  for exposures to  $\text{N}_2$ , air, and CDA (clean dry air) at 25, 100, 150, and 200°C are shown in Fig. 15. Crude ambient exposures were performed using a probe station. Focusing on the 25°C trace, it is seen ZnO NB devices are sensitive to ambient, even at room temperature. Response to either air or CDA exposure was qualitatively similar, with a decrease in the current and subsequent exposure to  $\text{N}_2$  resulting in partial to full recovery. In both cases, the mechanism for the current decrease

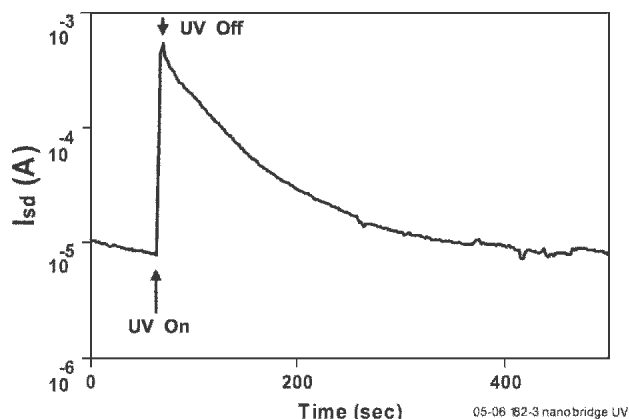


Fig. 14. Plot of current vs. time for 0.8- $\mu\text{m}$  comb device exposed to 375-nm UV light.

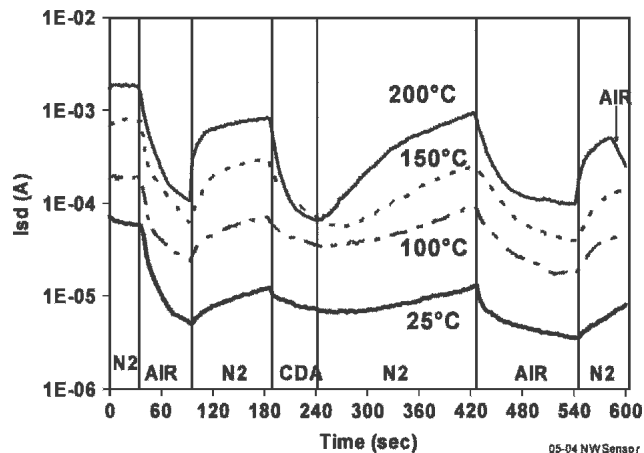


Fig. 15.  $I_{sd}$  vs. time for a 0.6- $\mu\text{m}$  comb structure operated with the microscope lamp on,  $V_{sd} = 15\text{ V}$ , and  $V_g = 10\text{ V}$  for exposures to  $\text{N}_2$ , air, and CDA at 25, 100, 150, and 200°C.

(increase) is likely oxygen adsorption (desorption) to (from) the surface which is accompanied by a reduction (increase) in electron carrier concentration.<sup>4,16,10,14</sup> One observed difference is that recovery from a CDA exposure appeared to be less rapid than recovery from air exposure. Moisture content in the air may explain this difference.

Examining the effects of temperature, it is seen that an increase in operating temperature resulted in a large increase in conductivity with  $I_{sd}$  increasing almost 2 orders of magnitude between 25 and 200°C. Although there is likely a component due to thermal generation of carriers, because the bandgap is about 3.3 eV, this cannot be dominant. Desorption of surface species such as  $\text{O}^-$  is likely the main component. Removal of oxygen from the surface results in a large increase in conductivity by freeing up electrons to contribute to conduction. Conductivity was observed to remain at elevated levels when devices were cooled down in  $\text{N}_2$ . Increased operation temperatures also resulted in improved recovery times. From 25 to 200°C, the steepness of the conductivity recovery slope after air or CDA exposure increases as the temperature is increased. This improvement was not unexpected. Metal oxide sensors are often operated at elevated temperatures due to the improved sensitivity and recovery brought about by enhanced redox reactions at the surface. Response times may also likely depend on partial pressures and electron concentration in the wire, which can be controlled<sup>16</sup> by the back gate. NB devices also showed sensitivity (not shown) to moisture (breath) and isopropyl alcohol, manifested as a rapid increase in conductivity at room temperature, consistent with previous reports.

A well-known problem with metal oxide sensors is sensor poisoning or a lack of recovery after exposure to an analyte.<sup>6</sup> Figure 16 shows plots of  $I_{sd}$  vs. time for a 0.6- $\mu\text{m}$  comb structure operated at 200°C with  $V_{sb} = 15\text{ V}$  and  $V_g = 10\text{ V}$  under repeated exposures to air with the probe station light either on or off. It is seen that the NB sensor is recoverable over many

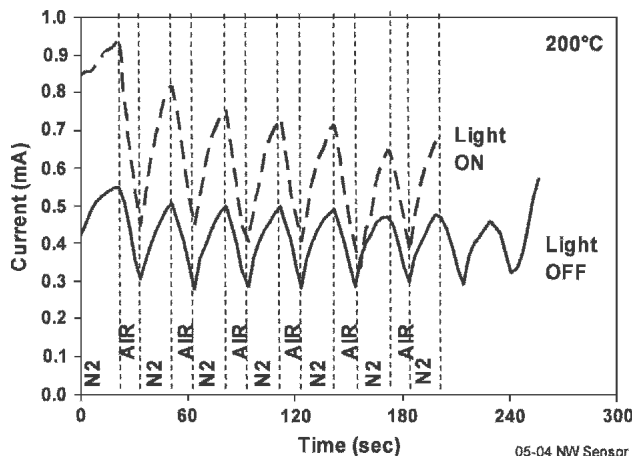


Fig. 16. Plots of  $I_{sd}$  vs. time for a 0.6- $\mu\text{m}$  comb structure operated at 200°C with  $V_{sb} = 15$  V and  $V_g = 10$  V under repeated exposures to air with probe station light either on or off.

cycles, suggesting that poisoning does not occur and confirming the plausibility of a potential gas-sensor application.

### SUMMARY AND CONCLUSION

Selective growth of high-quality ZnO NRs on a Si substrate without a metal catalyst was demonstrated using a patterned thin film of ZnO as a seed layer. ZnO NRs were found to have high crystal quality with a c-axis preference, vertical orientation, good alignment, and a strong sharp near-band edge UV PL at 380 nm without evidence of extrinsic visible-spectrum PL. Selective growth of NRs was observed on ZnO films from 1 to 80 nm thick deposited via both ALD and MOD. Other ZnO deposition methods likely may also be used as seed layers. The observed sensitivity of ZnO nanostructure morphology to ZnO seed-layer deposition technique and subsequent annealing conditions, as well as Si substrate implantation suggests the possibility of morphology control and optimization.

Using this catalyst-free selective growth technique, directed assembly and integration of working ZnO nanobridge UV/gas-sensor devices onto Si wafers was also achieved.<sup>34</sup> Directed assembly refers to the use of top-down techniques to pattern the forces (in this case a ZnO seed layer) that guide bottom up growth.<sup>7</sup> Integration implies that in addition to selective growth of NW in desired locations, NW are also connected to other desired locations to form electrically accessible devices. Several recent studies have demonstrated sensitivity of single-ZnO NW devices to  $\text{O}_2$ ,  $\text{H}_2\text{O}$ , ethanol, CO,  $\text{NO}_2$ ,  $\text{NH}_3$ , etc.<sup>4-6,10-18</sup> However, these devices were fabricated via “harvest and disperse,” a method not suitable for large-scale integration. The fact that our directly grown nanobridge structures can be operated as gas and UV sensors demonstrates the potential of the technique and represents a significant step toward practical large-scale integration of high-quality nanostructures into a Si CMOS-compatible microelectronics process flow.

### ACKNOWLEDGEMENTS

The authors thank Greg Stecker, Dr. Wei-wei Zhuang, Dr. Douglas Tweet, and Dr. Victor Hsu from Sharp Labs and Dr. Chun Fei and Prof. Jun Jaio from Portland State University for use of TEM equipment and assistance with imaging.

### REFERENCES

1. M. Huang, S. Mao, H. Feick, H. Yan, Y. Wu, H. Kind, E. Weber, R. Russo, and P. Yang, *Science* 292, 1897 (2001).
2. P. Yang, H. Yan, S. Mao, R. Russo, J. Johnson, R. Saykally, N. Morris, J. Pham, R. He, and H.J. Choi, *Adv. Funct. Mater.* 12 (5), 323 (2002).
3. Y.W. Heo, L.C. Tien, D.B.S. Kang, R. Ren, B.P. Gila, and S.J. Pearton, *Appl. Phys. Lett.* 85 (11), 2002 (2004).
4. H. Kind, H. Yan, B. Messer, M. Law, and P. Yang, *Adv. Mater.* 14, 158 (2002).
5. M.S. Arnold, P. Avouris, Z.W. Pan, and Z.L. Wang, *J. Phys. Chem. B* 107, 659 (2003).
6. A. Kolmakov and M. Moskovits, *Annu. Rev. Mater. Res.* 34, 151 (2004).
7. M. Law, J. Goldberger, and P. Yang, *Annu. Rev. Mater. Res.* 34, 83 (2004).
8. Y. Xia, P. Yang, Y. Sun, Y. Wu, B. Mayers, B. Gates, Y. Yin, F. Kim, and H. Yan, *Adv. Mater.* 15 (3), 353 (2003).
9. R. Konekamp, R.C. Word, and C. Schlegel, *Appl. Phys. Lett.* 85, 6004 (2004).
10. Q.H. Li, T. Gao, Y.G. Wang, and T.H. Wang, *Appl. Phys. Lett.* 86, 123117 (2005).
11. Y. Zhang, K. Yu, D. Jiang, Z. Zhu, H. Geng, and L. Luo, *Appl. Surf. Sci.* 242, 212 (2005).
12. Q. Wan, H. Li, Y.J. Chen, T.H. Wang, X.L. He, J.P. Li, and C.L. Lin, *Appl. Phys. Lett.* 84, 3654 (2004).
13. W.I. Park, J.S. Kim, G.C. Yi, M.H. Bae, and H.J. Lee, *Appl. Phys. Lett.* 85, 5052 (2004).
14. Q.H. Li, Q. Wan, Y.X. Liang, and T.H. Wang, *Appl. Phys. Lett.* 84, 4556 (2004).
15. Z. Fan and J.G. Lu, *Appl. Phys. Lett.* 86, 123510 (2005).
16. Z. Fan, D. Wang, P.C. Chang, W.Y. Tseng, and J.G. Lu, *Appl. Phys. Lett.* 85, 5923 (2004).
17. J.F. Conley, Jr., L. Stecker, and Y. Ono, *Nanotechnology* 16, 292 (2005).
18. C. Yu, Q. Hao, S. Saha, L. Shi, X. Kong, Z.L. Wang, *Appl. Phys. Lett.* 86, 063101 (2005).
19. H.T. Ng, J. Han, T. Yamada, P. Nguyen, Y.P. Chen, and M. Meyyappan, *Nano Lett.* 4, 1247 (2004).
20. Y.W. Heo, L.C. Tien, D.B.S. Kang, R. Ren, B.P. Gila, and S.J. Pearton, *Appl. Phys. Lett.* 85, 2002 (2004).
21. C.M. Lieber, *Mater. Res. Soc. Bull.* 28, 486 (2003).
22. S.Y. Li, P. Lin, C.Y. Lee, and T.Y. Tseng, *J. Appl. Phys.* 95, 3711 (2004).
23. H. Chik, J. Liang, S.G. Cloutier, N. Kouklin, and J.M. Xu, *Appl. Phys. Lett.* 84, 3376 (2004).
24. J. Kim, W.A. Anderson, Y.J. Song, and G.B. Kim, *Appl. Phys. Lett.* 86, 253101 (2005).
25. Y.H. Li, Y.T. Jang, and B.K. Ju, *Appl. Phys. Lett.* 86, 173103 (2005).
26. M.S. Islam, S. Sharma, T.I. Kamins, and R.S. Williams, *Nanotechnology* 15, L5 (2004).
27. R.S. Wagner and W.C. Ellis, *Appl. Phys. Lett.* 4, 89 (1964).
28. J. Jie, G. Wang, W.Y. Chen, X. Han, Q. Wang, B. Xu, and J.G. Hou, *Appl. Phys. Lett.* 86, 031909 (2005).
29. J.M. Jensen, A.B. Oelkers, R. Toivola, D.C. Johnson, J.W. Elam, and S.M. George, *Chem. Mater.* 14, 2276 (2002).
30. S. Muthukumar, H. Sheng, J. Zhong, Z. Zhang, N.W. Emanetoglu, and Y. Lu, *IEEE Trans. Nanotechnol.* 2, 50 (2003).
31. H. Yan, R. He, J. Pham, and P. Yang, *Adv. Mater.* 15, 402 (2003).
32. W. Lee, M.C. Jeong, and J.M. Myoung, *Nanotechnology* 15, 1441 (2004).
33. K. Vanheusden, W.L. Warren, C.H. Seager, D.R. Tallant, J.A. Voigt, and B.E. Gnade, *J. Appl. Phys.* 79, 7983 (1996).
34. J.F. Conley, Jr., L. Stecker, and Y. Ono, *Appl. Phys. Lett.* 87, 223114 (2005).